

Key immune regulators in retinal ischemia-reperfusion injury *via* RNA sequencing

Shan He¹, Cui-Ying Liu², Chang-Hong Ren³, Ting-Ting Meng¹, Heng Zhao⁴, Xu-Xiang Zhang¹

¹Department of Ophthalmology, Xuanwu Hospital, Capital Medical University, Beijing 100053, China

²School of Nursing, Capital Medical University, Beijing 100069, China

³Institute of Hypoxia Medicine, Xuanwu Hospital, Capital Medical University, Beijing 100053, China

⁴Beijing Institute of Brain Disorders, Capital Medical University, Beijing 100069, China

Correspondence to: Xu-Xiang Zhang. Department of Ophthalmology, Xuanwu Hospital, Capital Medical University, Beijing 100053, China. zhangxuxiang@vip.163.com; Heng Zhao. Beijing Institute of Brain Disorders, Capital Medical University, Beijing 100069, China. hengzhao@ccmu.edu.cn

Received: 2024-12-12 Accepted: 2025-02-13

Abstract

• **AIM:** To explore the immune cell infiltration and molecular mechanisms of retinal ischemia-reperfusion injury (RIRI) to identify potential therapeutic targets.

• **METHODS:** In the bulk RNA-seq analysis, This study performed differential gene expression analysis, weighted gene co-expression network analysis, and protein-protein interaction network analysis to identify hub genes. QuantSeq was used to determine the composition of infiltrating immune cells. Following the identification of hub genes, single-cell RNA-seq analysis was employed to pinpoint the specific immune cell types expressing these hub genes. Cell-cell communication analysis to explore signaling pathways and interactions between immune cells was further performed. Finally, the expression of these key immune regulators *in vivo* using quantitative real-time polymerase chain reaction (qRT-PCR) was validated.

• **RESULTS:** Bulk RNA-seq analysis identified *Stat2*, *Irf7*, *Irgm1*, *Igtp*, *Parp9*, *Irgm2*, *Nlrc5*, and *Tap1* as hub genes, with strong correlations to immune cell infiltration. Single-cell RNA-seq analysis further revealed six immune cell clusters, showing *Irf7* predominantly in microglia and *Tap1* in dendritic cells (DCs). And cell-cell communication analysis showed that microglia and DCs play central roles in coordinating immune activity. qRT-PCR validated the upregulation of these genes.

• **CONCLUSION:** In the acute phase of RIRI, *Irf7* and *Tap1* may be the potential therapeutic targets to reduce inflammation and promote neurological function recovery.

• **KEYWORDS:** retinal ischemia-reperfusion injury; immune cell infiltration; RNA sequencing; single-cell RNA sequencing; key immune regulators

DOI:10.18240/ijo.2025.07.06

Citation: He S, Liu CY, Ren CH, Meng TT, Zhao H, Zhang XX. Key immune regulators in retinal ischemia-reperfusion injury *via* RNA sequencing. *Int J Ophthalmol* 2025;18(7):1237-1251

INTRODUCTION

Retinal ischemia-reperfusion injury (RIRI) is a multifaceted and complex pathophysiological event characterized by a series of destructive processes triggered by the temporary loss and restoration of blood flow to the retina^[1-3]. This injury results in severe retinal damage, particularly to retinal ganglion cells, and is associated with a variety of ischemic retinal diseases such as glaucoma, retinal artery occlusion, and diabetic retinopathy^[4-5].

The pathogenesis of RIRI involves multiple damaging mechanisms, including oxidative stress, glutamate excitotoxicity, mitochondrial dysfunction, and inflammation^[6-8]. The ischemic phase leads to cell death primarily through necrosis, while the reperfusion phase triggers a cascade of inflammatory events, exacerbating the initial damage^[9-10]. The treatment of RIRI faces great challenges due to the complexity of the inflammation and immune responses.

In recent years, advances in high-throughput sequencing and bioinformatics have provided a large number of clues and evidence for the basic research of clinical diseases. Bulk RNA-seq is inexpensive and suitable for large-scale gene expression profiling, but it lacks cell type-specific resolution^[11]. Single-cell RNA sequencing (scRNA-seq) can provide higher resolution to reveal gene expression heterogeneity, cell type discrimination and cell state study at the single cell level, but it also has limitations such as high cost, technology noisy and low sequencing depth^[12-13]. There is a great need for effective integration and analysis of these data to discover key immune regulators and distinguish the heterogeneity of

immune cells. As such, a deeper understanding of the immune microenvironment after RIRI may be helpful for establishing the optimal new treatment strategy of various ischemic retinal diseases.

In this study we aimed to identify key immune regulators and for the acute phase of RIRI through bioinformatics. We extracted two datasets, bulk RNA-seq and scRNA-seq, from publicly available databases. First, for bulk RNA-seq data, we used weighted gene co-expression network analysis (WGCNA) and differentially gene expression screening to identify differentially co-expressed genes, evaluated immune cell infiltration using a deconvolution algorithm, and calculated the association between immune cell infiltration and hub genes. In addition, the scRNA-seq data further revealed the expression pattern of hub genes in each cell cluster. Finally, we successfully validated the expression of key immune regulators in mice.

MATERIALS AND METHODS

Ethics Approval The experiments of animals in this study were approved by the Ethics Committee of Capital Medical University (Approval number: AEEI-2024-232). All animal experiments were approved by the Intramural Animal Use and Care Committee of the Capital Medical University and were conducted in accordance with institutional guidelines.

Animal Model Adult male C57BL/6 mice (6-8wk, 18-20 g) were obtained from Vital River Laboratory Animal Technology Co. Ltd (Beijing, China).

We randomly divided the animals into two groups: 1) the ischemia-reperfusion (IR) group (RIRI model); 2) the control group (sham operation). The RIRI model was created as previously described^[14]. In brief, a 30-gauge needle filled with balanced salt solution was inserted into the anterior chamber to maintain intraocular pressure (IOP) at 70 mm Hg. In the sham operation, which served as the control, the same procedure was performed without raising the IOP. After 60min, the needle was carefully removed, allowing the IOP to return to normal.

Data Acquisition and Preprocessing The bulk RNA-Seq expression data of 16 samples, include 8 control samples and 8 IR samples (PRJNA859197). We first employed FastQC (version 0.12.1)^[15] to perform quality control on the raw sequence data and aggregate the results using MultiQC (version 1.15)^[16]. Next, we preprocessed the data with fastp (version 0.23.4) to trim low-quality bases and adapters^[17]. We then aligned the cleaned reads to the reference genome by HISAT2 (version 2.2.1)^[18], specifying strand-specific RNA-seq data. After alignment, we sorted and indexed the alignment files making use of samtools (version 1.17)^[19]. Finally, we quantified gene expression levels using featureCounts (version 2.0.6) for paired-end, strand-specific data, and exon-based counting^[20]. The mouse *GRCm39* gene set ([https://](https://www.ensembl.org/)

www.ensembl.org/), as the reference genome, was utilized to convert gene IDs to gene symbols in a matrix profile.

Identification of Differentially Expressed Genes and Functional Enrichment Analysis The differentially expressed genes (DEGs) between IR group and control group were analyzed using DESeq2 (v1.42.0)^[21]. A multitude of separate statistical tests for hypotheses were carried out on DEGs. Subsequently, a *P*-value was derived and adjusted using the FDR technique. The adjusted *P*-value was determined by applying the BH method for correction. To categorize DEGs of significant importance, the criteria include $|\log_2FC| \geq 2$ (FC: the fold change of expressions) and an adjusted $P \leq 0.01$. And the results were visualized with the ggplot2 package (version 3.4.4).

The enrichment analysis of Gene Ontology (GO) and Kyoto Encyclopedia of Genes and Genomes (KEGG) of DEGs were performed by clusterProfiler package (version 4.10.0)^[22]. We utilized the Benjamini-Hochberg method to control the false discovery rate for multiple hypothesis testing. A *P*-value ≤ 0.05 were considered statistically significant. Since enrichment analysis may output a redundancy list of significant terms with duplicate information, the rrvgo package was employed to simplify enrichment results^[23-24].

WGCNA WGCNA co-expression network were established using the WGCNA package^[25]. After removing the outlier genes, genes with the highest variability (top 50%) were selected as the input data for WGCNA. The optimal soft threshold power was selected to build a scale-free network. Subsequently, the adjacency matrix was converted into a topological overlap matrix for assessing the gene network connectivity. To further identify genes strongly associated with RIRI, the average linkage hierarchical clustering was applied for classifying genes with similar expression profiles by gene modules. The minimum number of genes required to form a module was 30 for the gene dendrogram. Ultimately, the relationships between the modules and clinical phenotype were estimated through Pearson correlation analysis, and the modules with highest correlation coefficient were selected for further research.

Construction of Protein-protein Interaction Network We intersected genes in the key modules of WGCNA and DEGs. The intersecting genes were uploaded to the Search Tool for the Retrieval of Interacting Genes (STRING) database (<https://cn.string-db.org/>) to identify those with strong correlations, setting the medium confidence set to 0.4. For protein-protein interaction (PPI) establishment, all seven active interaction sources (text-mining, experiments, databases, co-expression, neighborhood, gene fusion and co-occurrence) were used. Then, Cytoscape 3.9.1 (<https://cytoscape.org>) from National Resource for Network Biology was used to construct the PPI

Table 1 The primers for qRT-PCR

Parameters	<i>lrf7</i>	<i>Tap1</i>
Sequence (forward)	CTT CAG CAC TTT CTT CCG AGA	GAA GCT TCA GTT CAC CCA
Sequence (reverse)	TGT AGT GTG GTG ACC CTT GC	CAC AAG GCC TTT CAT GTT TG
NCBI gene accession number	NM_016850.3	NM_001161730.1
Primer location (nucleotide position)	F: 789-808; R: 928-909	F: 518-1535; R: 1677-1658
Intron/exon location	exon 4, 6	exon 6-8

qRT-PCR: Quantitative real-time polymerase chain reaction.

network based on the protein interaction data obtained from STRING and to calculate their degree values. After selecting the largest subnetwork, the top genes were picked as hub genes based on their maximal clique centrality (MCC) rankings after computing the PPI network in CytoHubba (version 0.1).

Analysis of Immune Infiltration and Correlation with Hub Genes We used quanTIseq algorithm, which applies constrained least square regression, to assess the relative abundance of 10 distinct immune cells by using the IOBR tool^[26-27]. In addition, we used the Wilcoxon rank sum test, provided by the stats package (version 4.2.1), to assess the differences in immune infiltration, which were visualized with the Violin Plot. Furthermore, we calculated the Spearman correlation coefficient for each immune cell type and presented the results with a correlation heatmap. We also visualized the correlation coefficients between the identified hub genes and immune cells using Lollipop charts.

scRNA-seq Data Analysis We used the Seurat package to analyze scRNA-seq data (PRJNA859197), including 3 control samples and 3 IR samples. For downstream analyses, we excluded cells with genes expressed in less than 5 cells and a total number of expressed genes less than 300. Subsequently, data normalization and scaling were conducted, followed by the identification of 2000 highly variable genes. Principal component analysis was applied for dimensionality reduction, and the Harmony algorithm was used for batch effect correction^[28]. Cells were clustered based on their gene expression profiles, and clusters were annotated with biological cell types. The DimPlot function was used to visualize cell clusters in reduced-dimensional space, while FeaturePlot function overlaid gene expression levels on this space to show where specific genes are expressed across clusters. Finally, the cellular crosstalk was calculated with CellChat package^[29].

Electroretinogram Electroretinogram (ERG) was performed 24h after retinal reperfusion in mice using the Espion Visual Electrophysiology System (Diagnosys, USA), referring to the previous method of our group^[30]. The pupils were dilated with 0.5% tropicamide and 0.5% phenylephrine hydrochloride (Mydrin-P, Santen Pharmaceutical, Osaka, Japan). The mice were kept warm in the prone position throughout the recording

process. ERG was recorded by means of a golden ring that made contact with the corneal surface through a layer of 0.2% carbomer. Additionally, needle electrodes were inserted into the cheeks and tails of animals and served as the reference and ground leads, respectively. First, after 12h of dark adaptation, the scotopic ERG was recorded with light stimulation of 0.01 cd·s/m² and 20 cd·s/m² respectively; then after 15min of light adaptation, the photopic ERG was recorded using a light stimulation of 20 cd·s/m² against a white background (100 cd·s/m²). Finally, light-adapted 10 Hz flicker ERG was recorded.

Hematoxylin-Eosin Staining of Retina Whole globes were immersion fixed in 4% PFA overnight at 4°C, followed by paraffin processing. Eyes were sectioned at 6 μm and stained with hematoxylin and eosin (H&E). Entire retinas were imaged, ora serrata to ora serrata through the optic nerve head.

Quantitative Real-Time Polymerase Chain Reaction Total RNA was extracted from the retinas with the MolPure[®] Cell/Tissue Total RNA Kit (Yeasten) according to the manufacturer's instructions. cDNA was synthesized with the NovoScript[®] Plus All-in-one 1st Strand cDNA Synthesis SuperMix (Novoprotein) according to a standard protocol. Quantitative analysis was conducted by the Light Cycler 480 real-time PCR system (Roche Molecular Systems, Inc., SUR). The expression of target mRNAs was measured and normalized to that of β-actin. Finally, fold change was calculated with 2^{-ΔΔCt} method. The primers are summarized in Table 1.

Statistical Analysis Statistical analyses were conducted using R software (version 4.3.2) and the GraphPad Prism software (version 10.0). All tests were two-sided, and a *P*-value <0.05 was considered statistically significant.

RESULTS

The study flow chart is shown in Figure 1.

DEGs in RIRI Linked to Inflammation and Immune Regulation Through GO and KEGG Pathways To identify genes with altered expression in RIRI, differential gene expression analysis was conducted. We identified a total of 707 DEGs between 8 IR samples and 8 control samples with the screening criteria of an adjusted *P*≤0.01 and |log₂FC|≥2. Among these DEGs, 606 genes were found to be up-regulated while 101 genes were down-regulated (Figure 2A). A heatmap

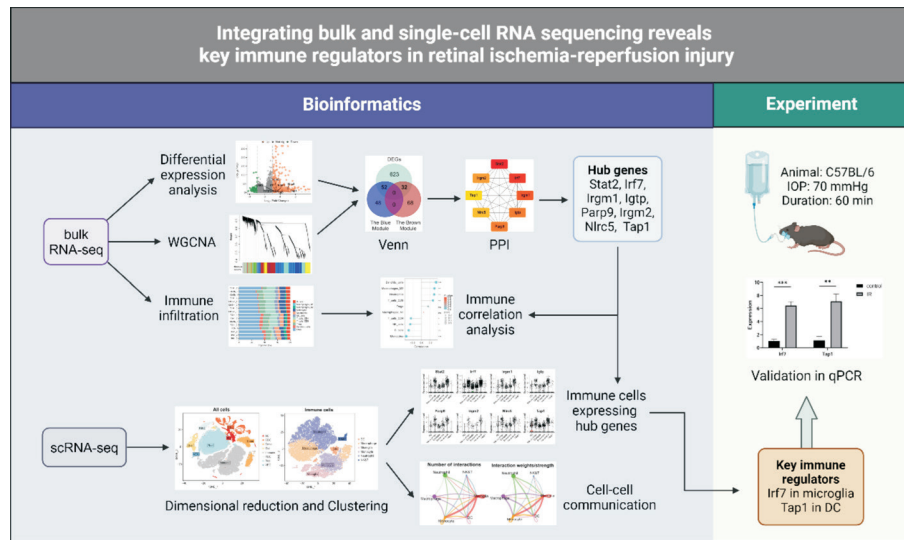


Figure 1 Flow diagram of the study DC: Dendritic cell; IOP: Intraocular pressure; PPI: Protein-protein interaction; WGCNA: Weighted gene co-expression network analysis; qPCR: Quantitative real-time polymerase chain reaction.

was created to visualize DEGs expression patterns, which underscored the distinct transcriptional landscape induced by RIRI (Figure 2B). These DEGs were further analyzed to understand the biological processes and pathways involved. GO and KEGG enrichment analyses were performed to provide insights into the underlying biological functions and pathways.

The results of the GO functional analysis included biological processes, cellular components, and molecular functions, with a total of 2153 GO terms identified. The 20 most significant terms were displayed in a bubble plot (Figure 2C). To address redundancy among the GO terms, we simplified the list based on semantic similarity and visualized it in a treemap (Figure 2D). The analysis revealed that the DEGs are predominantly involved in several biological processes, including leukocyte proliferation, epithelial morphogenesis, negative regulation of leukocyte activation, negative regulation of immune system processes, regulation of the extracellular regulated protein kinase 1 (ERK1) and ERK2 cascade, regulation of hemopoiesis, and cytokine-mediated signaling pathways.

A total of 90 KEGG pathways were obtained. Among them, the most significant 20 pathways were displayed on the bubble plot and summarized by category shown in the bar graph (Figure 2E-2F). The KEGG pathways revealed significant involvement in immune-related pathways, including tumor necrosis factor (TNF) signaling pathway, cytokine-cytokine receptor interaction, JAK-STAT signaling pathway, Viral protein interaction with cytokine and cytokine receptor, C-type lectin receptor signaling pathway, Complement and coagulation cascades and nuclear factor (NF)-kappa B signaling pathway. Together, these analyses revealed these DEGs, which not only exhibited markedly changed expression in the disease but also had a significant correlation with inflammation.

WGCNA Identifies Gene Modules Strongly Linked to RIRI and Potential Therapeutic Targets WGCNA was used to identify gene sets with strong covariation in RNA-seq samples, revealing gene modules linked to RIRI and potential biomarker or therapeutic target genes. Hierarchical clustering found no outlier samples (Figure 3A). The top 50% of genes with the highest variance were selected, and a soft threshold of $\beta=3$ (scale-free $R^2=0.911$) was chosen to build the network (Figure 3B). Seven gene modules were identified (Figure 3C), and heatmaps showed the topological overlap and module relationships (Figure 3D-3E). The blue, brown, and turquoise modules were strongly associated with RIRI, with the blue and brown modules showing the highest correlation (0.81 and 0.89, $P<e-200$; Figure 3F-3G). The top 100 genes from these modules were selected for further study.

WGCNA and DEGs integration identifies hub genes in RIRI After combining WGCNA and DEGs results, 84 differentially co-expressed RIRI genes were identified (Figure 4A). GO analysis showed these genes are involved in immune response pathways (Figure 4B). PPI analysis revealed a network of 81 nodes and 190 edges, and the largest subnetwork (55 nodes) were selected for subsequent analysis (Figure 4C). We identified 8 hub genes: *Stat2*, *Irf7*, *Irgm1*, *Igtp*, *Parp9*, *Irgm2*, *Nlrc5*, and *Tap1* (Figure 4D). These genes were significantly elevated in the IR group (Figure 4E).

Deconvolution Analysis Identifies Coordinated Immune Cell Infiltration in RIRI Retinas In order to provide valuable insights into the composition and function of infiltrating immune cells, QuantIseq was based on deconvolution algorithm for RNA-seq data to quantify the distinct 10 immune cell types within the samples. These immune cells included B cell, M1 macrophage, M2 macrophage, monocyte, neutrophil, natural killer cell (NK), CD4 T cell, CD8 T cell,



Figure 2 Comprehensive gene expression and enrichment analysis of RIRI A: The volcano plot illustrated DEGs between RIRI and control samples, highlighting significant upregulated (orange) and downregulated (green) genes. B: The heatmap displayed DEGs across samples, distinguishing expression patterns between RIRI and control groups. C: The bubble plot depicted the top 20 enriched GO terms for biological processes, with bubble size indicating the number of genes and color reflecting enrichment significance (FDR). D: The treemap simplified GO terms by grouping similar biological processes based on semantic similarity, offering a clearer overview of key functions involved in RIRI. E: The bubble plot showed the top 20 enriched KEGG pathways linked to DEGs, where bubble size represented the number of genes, and color indicates significance. F: The bar graph categorized the top 20 enriched KEGG pathways by pathway types, such as environmental information processing and human diseases, emphasizing their biological relevance to RIRI. RIRI: Retinal ischemia-reperfusion injury; DEGs: Differentially expressed genes; GO: Gene Ontology; KEGG: Kyoto Encyclopedia of Genes and Genomes.

regulatory T cell and dendritic cell (DC). The Stacked bar chart with dendrogram revealed the proportion of all kinds of immune cells between samples (Figure 5A). As shown in the violin plot, we compared the percentage of various immune cell infiltration in IR and control retinas (Figure 5B). There was a marked increase in the proportion of M2 macrophage, neutrophils, CD8 T cells and DC in IR group. Furthermore, the correlation analysis of the 10 immune cell types was conducted

(Figure 5C). Interestingly, B cell, M2 macrophage, monocyte, neutrophil, NK, CD4 T cell, CD8 T cell and DC exhibit strong correlations with each other, indicating a coordinated and interconnected immune response in RIRI retinas.

Hub Genes Correlation with Diverse Immune Cells in RIRI

To clarify the relationship between hub gene and RIRI immune cell infiltration, we investigated the correlation between the hub genes and immune cells. The hub genes displayed little

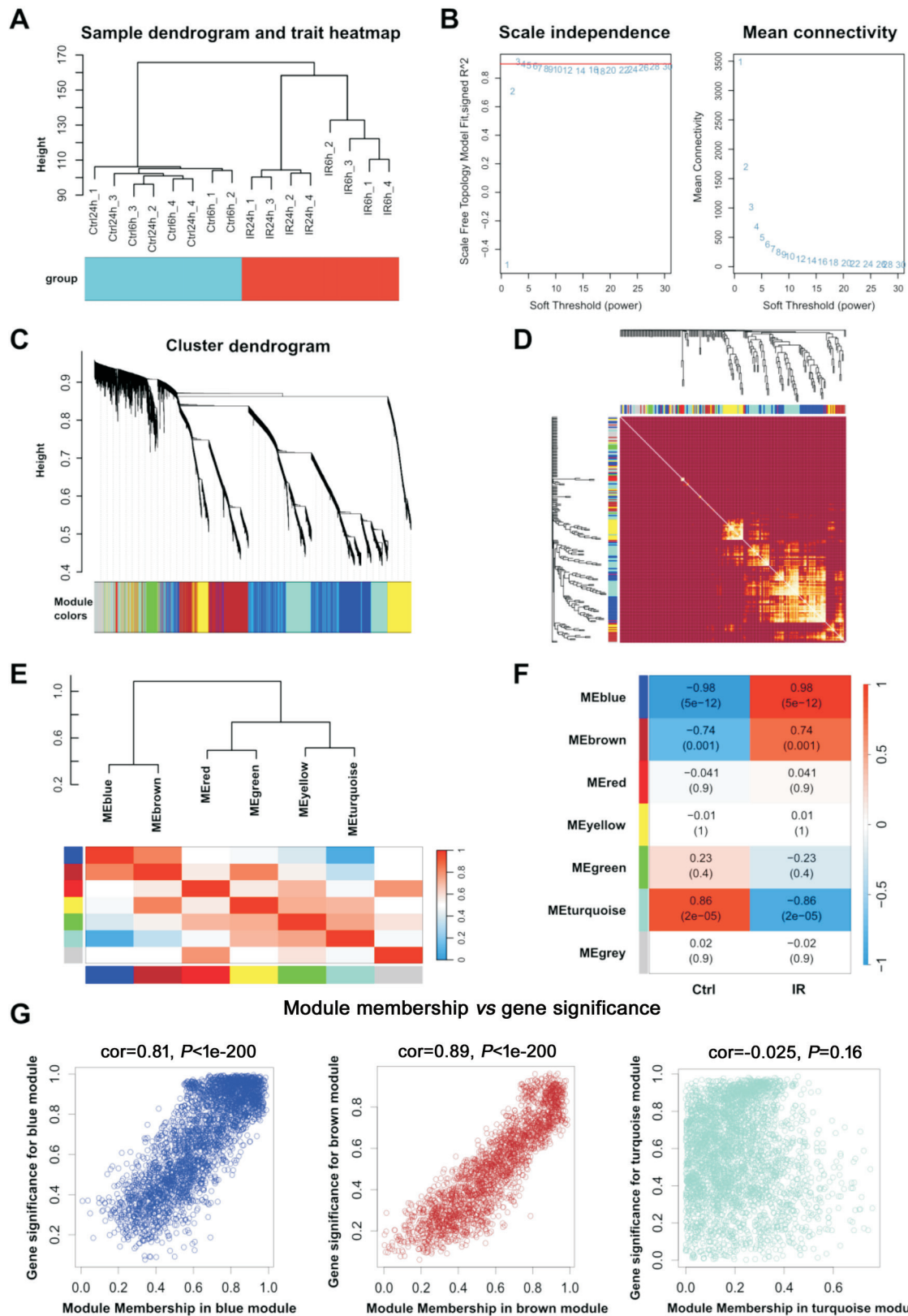


Figure 3 Identification of key modules by WGCNA A: Sample dendrogram and trait heatmap showing hierarchical clustering of IR and control samples based on gene expression profiles. B: Plots for scale independence and mean connectivity across different soft threshold powers to select the appropriate power for WGCNA. C: Cluster dendrogram of genes, with each color representing a distinct co-expression module. D: Heatmap displaying the topological overlap matrix for gene co-expression relationships. E: Module correlation heatmap showing relationships among identified modules. F: Heatmap representing the module-trait relationships, where each cell's upper value is the correlation coefficient, and the lower value is the *P*-value. G: Scatter plots showing the relationship between module membership and gene significance for the three most significant modules: blue, brown, and turquoise, with correlation coefficients and *P*-values. WGCNA: Weighted gene co-expression network analysis.

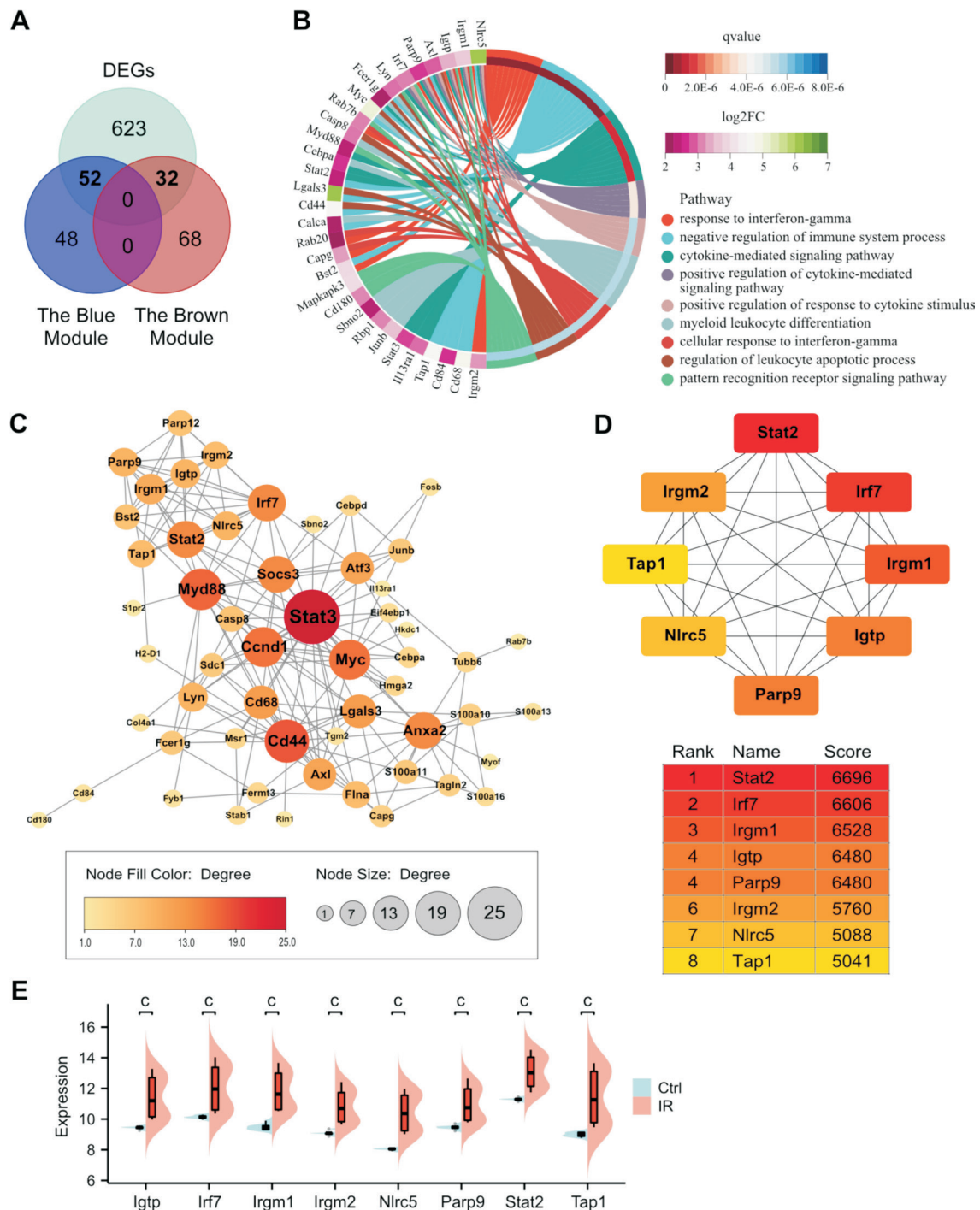


Figure 4 Identification of hub genes by PPI A: Venn diagram showing the overlap between DEGs, the brown module, and the blue module; B: Chord diagram representing the top 9 enriched GO terms associated with the intersecting genes, with links between genes and their respective biological processes; C: PPI network of intersecting genes, highlighting key nodes based on their degree of connectivity; D: Identification of 8 hub genes (*Stat2*, *Irf7*, *Irgm1*, *Igtp*, *Parp9*, *Irgm2*, *Nlrc5*, and *Tap1*) from the PPI network, ranked by their importance using the MCC algorithm; E: Violin plots showing the expression levels of the 8 hub genes in the IR and control groups, with significant differences indicated by ^cP<0.001. PPI: Protein-protein interaction; MCC: Maximal clique centrality; DEGs: Differentially expressed genes; GO: Gene Ontology; IR: Ischemia-reperfusion; Ctrl: Control group.

or no correlation with M1 macrophage and regulatory T cell. However, a significant correlation was observed between the hub genes and a wide variety of immune cells (Figure 6A-6H). These results suggest that the varied expression levels of hub genes have a unique effect on the immune infiltration of RIRI.

scRNA-seq and Bulk RNA-seq Identify *Irf7* and *Tap1* as RIRI Therapeutic Targets We conducted scRNA-seq analysis to further clarify the specific roles of immune cells in RIRI, which provided a high-resolution view of hub gene expression within distinct immune cell subclusters and

Key immune regulators in RIRI

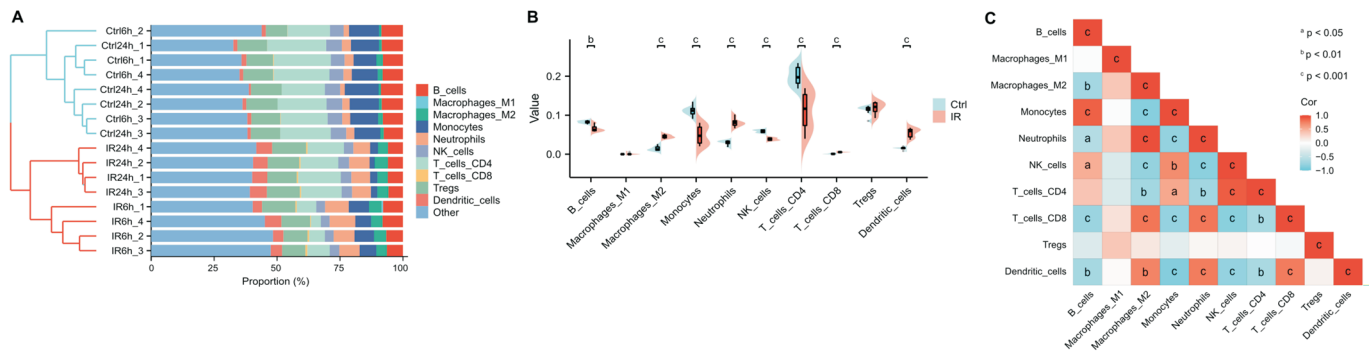


Figure 5 Analysis of immune infiltration A: Stacked bar chart showing the proportions of different immune cell types across samples, with hierarchical clustering distinguishing between control and IR groups; B: Violin plots comparing the proportions of various immune cell types between the IR and control groups, with significant differences; C: Heatmap showing correlation analysis between different immune cell types, with color indicating the strength and direction of the correlation. IR: Ischemia-reperfusion; Ctrl: Control group; NK: Natural killer; Tregs: Regulatory T cell.

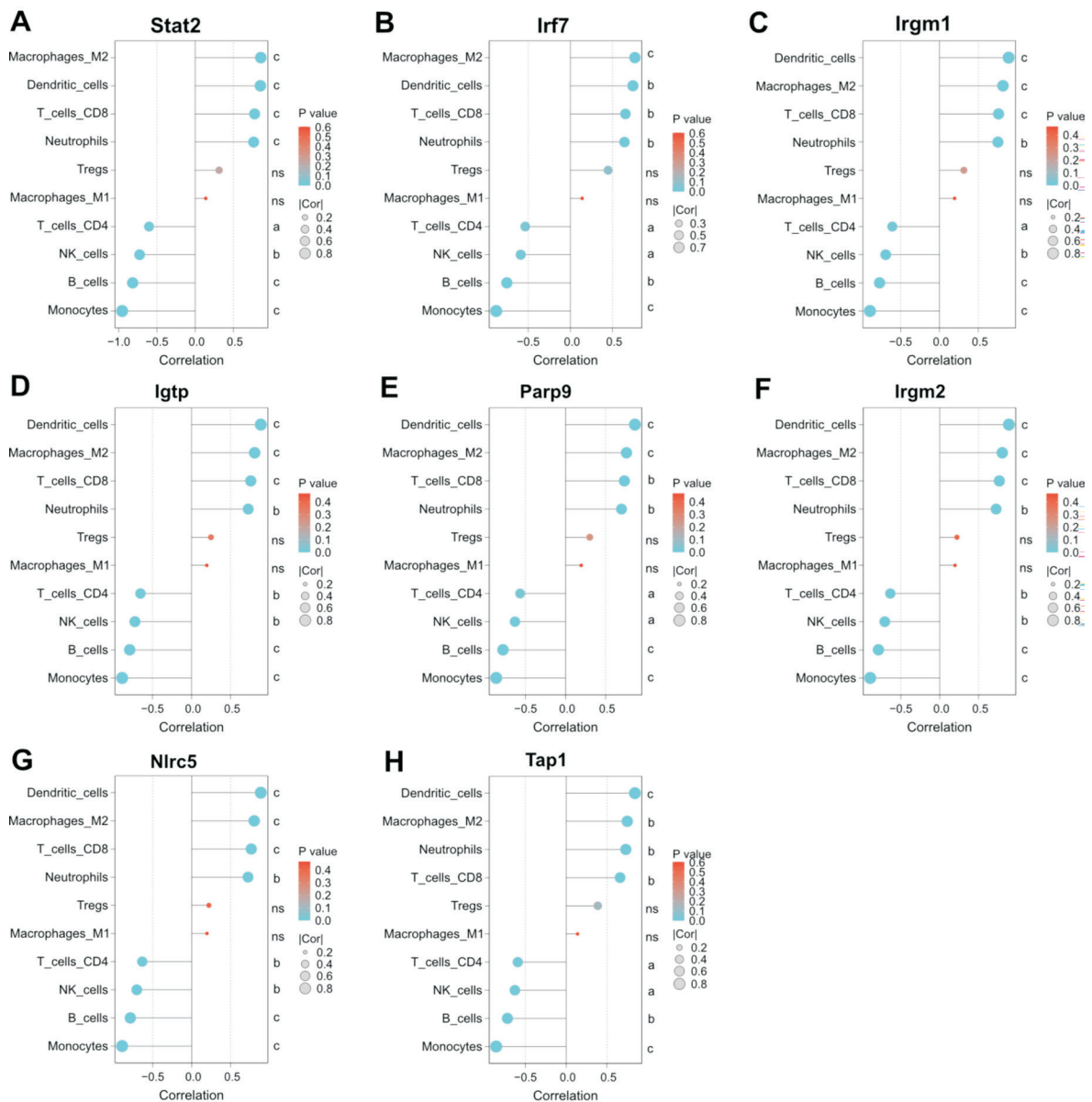


Figure 6 Correlation between hub genes and infiltrating immune cells Correlation analysis of *Stat2*, *Irf7*, *Irgm1*, *Igtp*, *Parp9*, *Irgm2*, *Nlrc5*, and *Tap1* with various immune cell types. The size of the dots represents the strength of the correlation (correlation coefficient), while the color gradient indicates the significance of the *P*-value. ^a*P* < 0.05, ^b*P* < 0.01, and ^c*P* < 0.001. ns: Not significant.

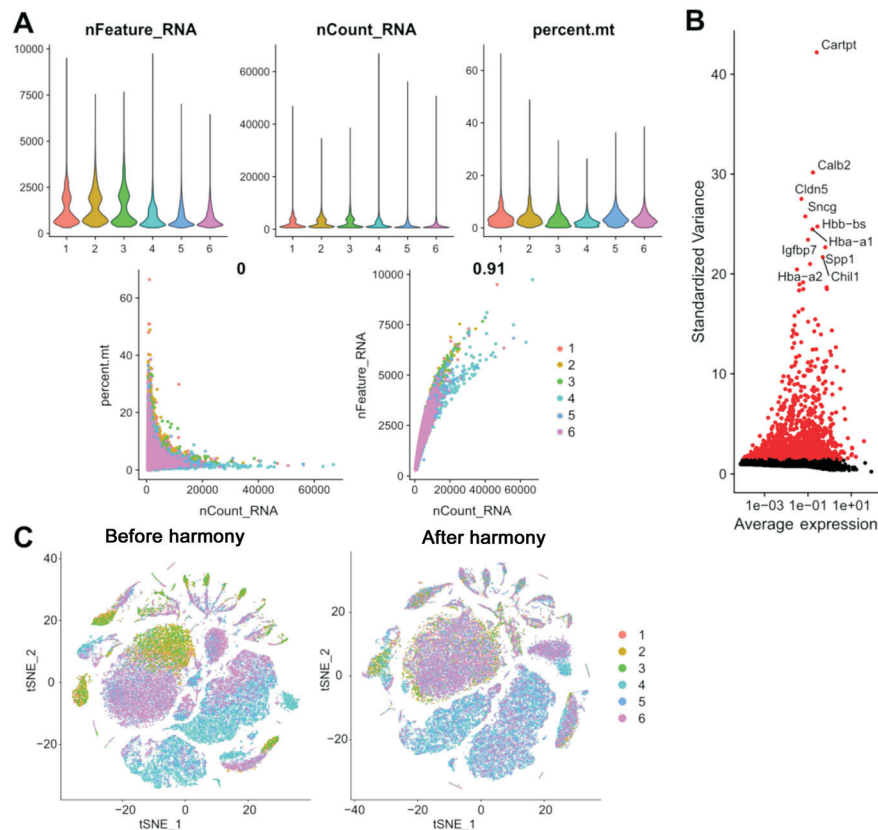


Figure 7 Quality control and integration of scRNA-seq dataset A: Quality control plots showing cell sample reliability, including nFeature_RNA, nCount_RNA, and percent.mt distributions across six sample groups. Scatter plots depict the relationship between nCount_RNA and percent.mt, and between nCount_RNA and nFeature_RNA, with correlation values shown. B: Volcano plot of the 2000 most highly variable genes, highlighting the top 10 genes in red. C: t-SNE plots demonstrating the distribution of different samples before and after applying the harmony embedding for data integration. Sample 1-3: Control group; Sample 4-6: IR group.

uncovered the cell-cell communication networks driving the immune response. After integrating data from control (16 927 cells) and IR groups (45 767 cells), a total of 62 694 cells were identified. Quality control was performed using gene count, UMI count, and mitochondrial gene percentage (Figure 7A). Harmony integration was applied to correct batch effects, leading to a more uniform mix of cells from different samples (Figure 7C). t-SNE analysis revealed eight major cell clusters, including rods, cones, bipolar cells, Müller cells, astrocytes, endothelial cells, and immune cells based on canonical markers and the most variable upregulated genes (Figures 8A, 9A). Given the strong connection between hub genes and immune cells from the bulk RNA-seq analysis, 20 320 immune cells expressing *Ptpcr* (CD45) were isolated for further investigation (Figure 9C). These immune cells were grouped into six subclusters: microglia, monocytes, macrophages, neutrophils, DC, and NK&T cells (Figures 8B, 9B). The expression levels of the eight hub genes (*Stat2*, *Irf7*, *Irgm1*, *Igtp*, *Parp9*, *Irgm2*, *Nlrc5*, *Tap1*) across these immune subclusters were visualized through violin and t-SNE plots (Figure 9D).

Irf7 was predominantly expressed in microglia, indicating its crucial role in microglial activation and pro-inflammatory

responses during RIRI. Similarly, *Tap1* was mainly expressed in DC, suggesting its involvement in antigen presentation and immune activation. These findings align with the bulk RNA-seq data, confirming that *Irf7* and *Tap1* are key regulators of immune responses in RIRI.

To further explore how immune cells coordinate in RIRI, CellChat was used to analyze cell-cell communication, focusing on the secretion patterns of immune cells based on ligand-receptor interactions. Significant interactions were observed between microglia and other immune cells like monocytes and DCs, with microglia showing interactions with all immune cell types (Figure 10A). A Sankey plot depicted three major outgoing communication patterns: Microglia were primarily involved in Pattern 2, which included pathways like secreted phosphoprotein 1 (SPP1), galectin, and complement, highlighting their role in tissue repair and immune recruitment. DCs were associated with Pattern 3, driven by the chemokine (C-X-C motif) ligand (CXCL), which is crucial for recruiting and activating other immune cells (Figure 10B). Other immune cells participated in Pattern 1, which involved chemokine (C-C motif) ligand (CCL), macrophage migration inhibitory factor (MIF), and TNF, indicating their role in propagating inflammation.

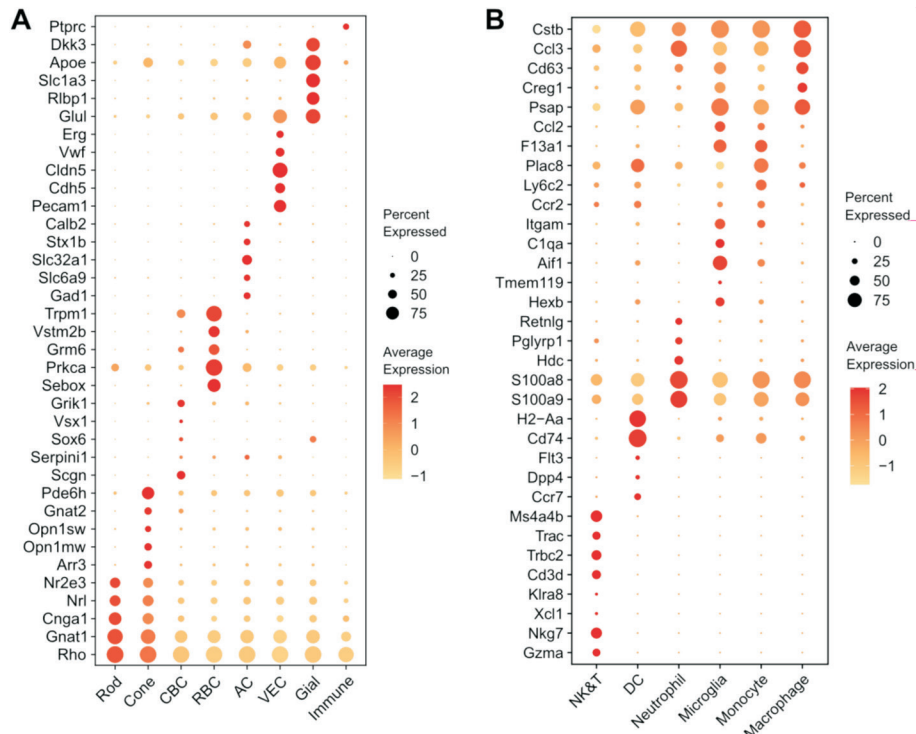


Figure 8 Clustering strategy of cell populations A: Heatmap displaying the scaled expression values of canonical markers defining major retinal clusters. B: Heatmap showing the scaled expression values of markers defining various immune cell clusters. AC: Amacrine cells; CBC: Cone bipolar cells; Cone: Cone photoreceptors; Gial: Glial cells; Immune: Immune cells; RBC: Rod bipolar cells; Rod: Rod photoreceptors; VEC: Vascular endothelial cells; DC: Dendritic cells; NK&T: Natural killer and T cells.

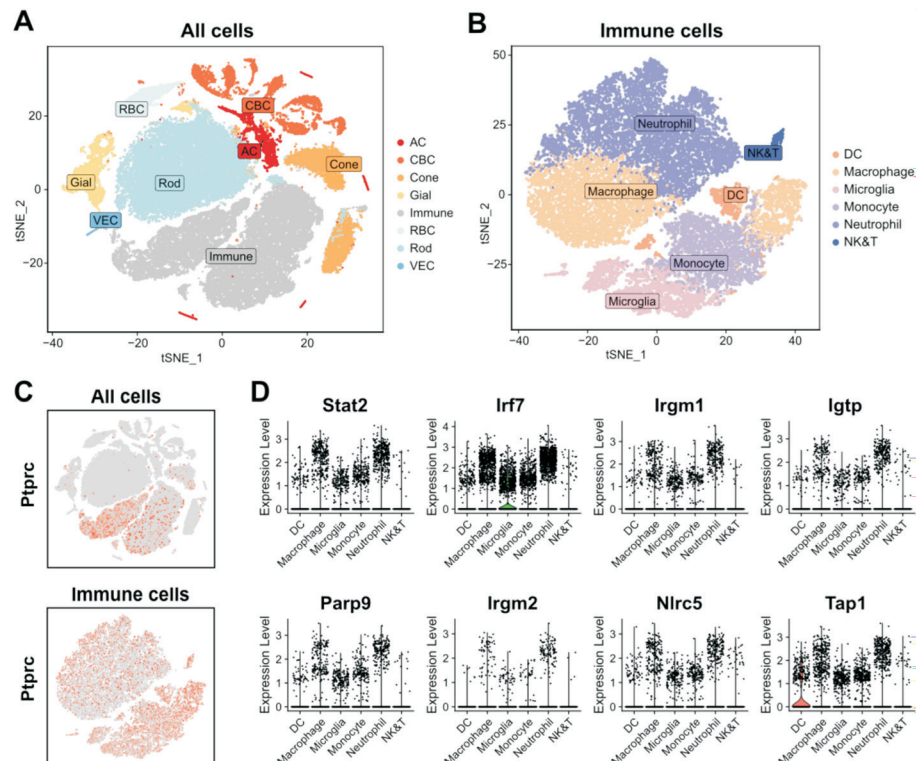


Figure 9 scRNA-seq analysis of RIRI A: t-SNE plot showing the clustering of all retinal cells from control and IR groups, with distinct cell types labeled (AC, CBC, Cone, Glial, Immune, RBC, Rod, VEC); B: t-SNE plot showing six immune cell subclusters, including DC, macrophages, microglia, monocytes, neutrophils, and NK&T cells; C: Expression of *Ptprc* in all retinal cells and specifically in immune cell clusters; D: Violin plots displaying the expression levels of 8 hub immune genes (*Stat2*, *Irf7*, *Irgm1*, *Igtp*, *Parp9*, *Irgm2*, *Nlrc5*, *Tap1*) across the immune cell subclusters. AC: Amacrine cells; CBC: Cone bipolar cells; Cone: Cone photoreceptors; Glial: Glial cells; Immune: Immune cells; RBC: Rod bipolar cells; Rod: Rod photoreceptors; VEC: Vascular endothelial cells; DC: Dendritic cells; NK&T: Natural killer and T cells; RIRI: Retinal ischemia-reperfusion injury; IR: Ischemia-reperfusion.

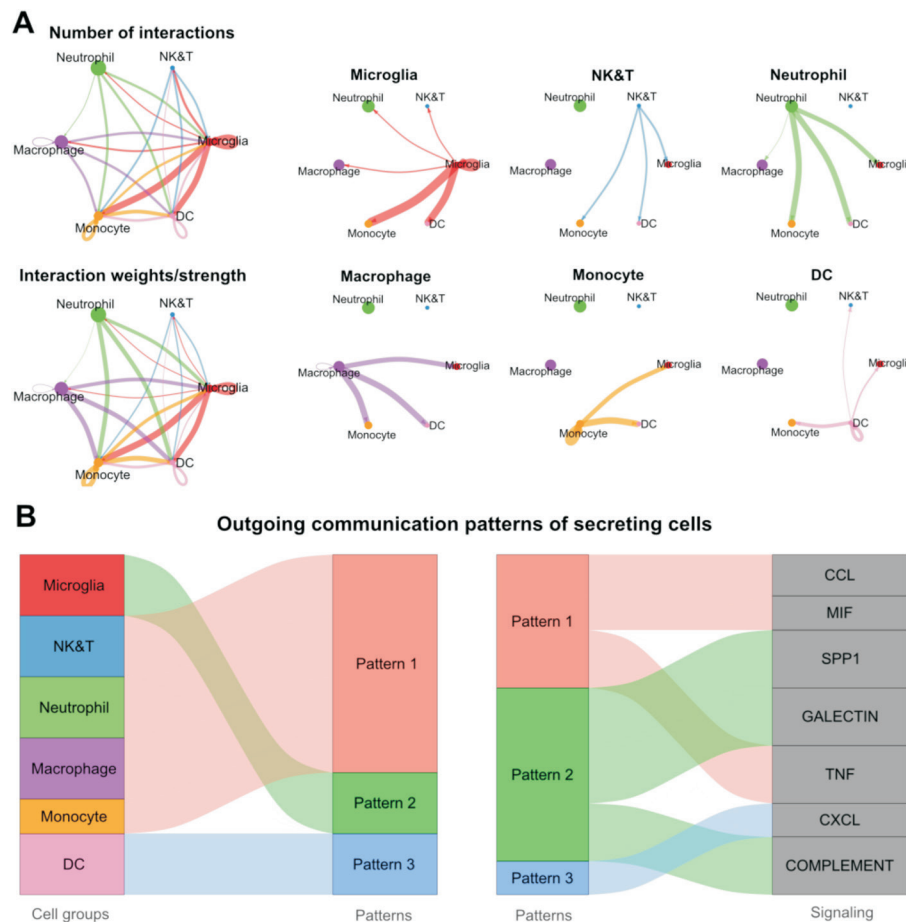


Figure 10 Cell-cell communication patterns in RIRI A: The number and strength of interactions between six immune cell subclusters: microglia, NK&T cells, neutrophils, macrophages, monocytes, and DC. B: Sankey plots illustrating the inferred outgoing communication patterns of secreting cells, linking specific cell groups to signaling patterns and associated signaling molecules. CCL: Chemokine (C-C motif) ligand; MIF: Macrophage migration inhibitory factor; SPP1: Secreted phosphoprotein 1; TNF: Tumor necrosis factor; CXCL: Chemokine (C-X-C motif) ligand; RIRI: Retinal ischemia-reperfusion injury; DC: Dendritic cells; NK&T: Natural killer and T cells.

This scRNA-seq analysis complements the bulk RNA-seq findings by providing cellular-level detail, showing how hub genes identified in the bulk analysis, particularly *Irf7* and *Tap1*, are specifically expressed in different immune cell subtypes and how these cells communicate during RIRI. These results offer a deeper understanding of the immune cell infiltration in RIRI and highlight *Irf7* and *Tap1* as potential therapeutic targets for modulating immune responses to improve recovery.

qRT-PCR Confirm Expression of *Irf7* and *Tap1* in RIRI

To further confirm the findings from the bulk and scRNA-seq analyses, we successfully established the RIRI model. The edema of the cornea, the decrease of ERG amplitude, the thinning of retinal thickness and the loss of ganglion cells in HE staining indicated the successful establishment of the RIRI model (Figure 11A-11C). Quantitative real-time polymerase chain reaction (qRT-PCR) were employed to validate the expression of *Irf7* and *Tap1* in RIRI. The qRT-PCR validation results showed that both *Irf7* and *Tap1* were significantly upregulated in the IR group one day after RIRI (Figure 11D).

DISCUSSION

In this study, by applying WGCNA, differential gene expression analysis, and PPI analysis of bulk RNA-seq data, we identified 8 hub genes (*Stat2*, *Irf7*, *Irgm1*, *Igtp*, *Parp9*, *Irgm2*, *Nlr5* and *Tap1*) that are significantly associated with RIRI. To complement this, we performed scRNA-seq analysis, which revealed that *Irf7* is predominantly expressed in microglia and *Tap1* in DC, confirming their roles in inflammation and immune activation during RIRI. We also found increased infiltration of immune cells, such as M2 macrophages, neutrophils, CD8 T cells, and DC, in the IR group, indicating a complex immune response. Through cell-cell communication analysis, we showed that microglia and DC play central roles in coordinating immune activity. Finally, we validated the upregulation of *Irf7* and *Tap1* using qRT-PCR. Together, our bulk RNA-seq and complementary scRNA-seq analysis suggest that *Irf7* and *Tap1* are potential therapeutic targets for modulating immune responses in RIRI.

RIRI frequently results in irreversible neurological damage to the retina and profoundly affects the socioeconomic status

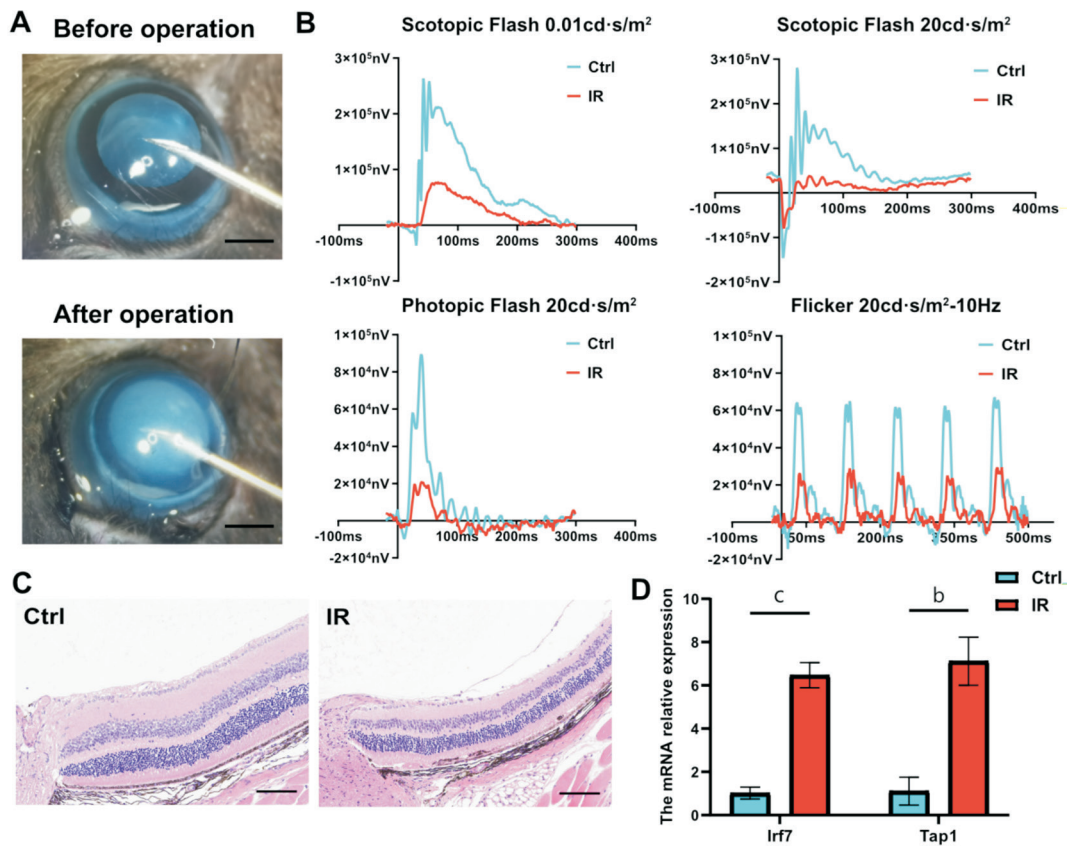


Figure 11 Validation of *Irf7* and *Tap1* in control and IR groups A: Eyeballs of mice under the microscope before and after operation, scale bar=1000 μ m; B: Electroretinogram in different modes in the control and IR groups; C: HE staining of retinas from control and IR groups, scale bar=100 μ m. D: Expression levels of *Irf7* and *Tap1* in control and IR groups. IR: Ischemia-reperfusion; Ctrl: Control group; HE: Hematoxylin-eosin. ^b $P < 0.01$; ^c $P < 0.001$.

of both patients and the healthcare system^[31-33]. However, its specific mechanisms remain to be explored. The severity and prognosis of RIRI has been determined to be significantly controlled by inflammation and immune infiltration^[34]. The immune cell infiltration provides valuable insights into the forecasting disease progression and therapeutic efficacy by understanding the role of immune cells in the microenvironment^[14,35]. Moreover, the composition and phenotype of immune cells are also altered depending on the degree and stage of injury. Therefore, combining bioinformatics and integrating the data of existing studies to study the inflammatory and immune response of RIRI is an urgent need and of great significance.

To our best knowledge, this study is the first to integrate transcriptomics data from both bulk RNA-seq and scRNA-seq to explore the molecular mechanisms underlying RIRI at both the whole tissue and single-cell levels. This approach allowed us to gain a comprehensive understanding of the immune cell infiltration and identify potential therapeutic targets.

To further elucidate the roles of these key immune regulators, we will discuss the mechanisms and functions of *Irf7* and *Tap1* in the immune response to RIRI in detail. *Irf7*, interferon regulatory factor 7, belongs to the interferon regulatory factor family and is one of the major regulators of type I interferon

production. It plays a key role in antiviral immune response and a variety of autoimmune diseases^[36-37]. *Irf7* expression is upregulated not only in RIRI, but also in retinal inflammation caused by other diseases such as macular degeneration and retinal detachment^[38]. *Irf7* is a critical transcription factor regulating microglial activation, particularly through the pro-inflammatory (M1) and anti-inflammatory phenotype (M2) polarization balance, playing roles in neuroinflammation, spinal cord injury response, neurodegeneration, and tumor environments^[39-46]. Under physiological conditions, microglia are exposed to high levels of transforming growth factor β 1 (TGF β 1) in the brain, leading to low expression of *Irf7*, which keeps microglia in a relatively inactive state (M0)^[39]. Upon injury or inflammation, the expression of *Irf7* increases, promoting a M1 state in microglia^[41-42]. Conversely, its downregulation promotes the phenotypic switch of microglia from M1 to M2, promoting anti-inflammation and tissue repair^[40,44]. Similarly, we also found that *Irf7* expression increased in the IR group, especially in microglia, during the acute phase of RIRI (Figures 4E, 6B, 9D). This suggests that high *Irf7* expression is a switch for microglia activation and M1 polarization during the acute phase of RIRI. Moreover, our research found that microglia, the resident immune cells of the central nervous system, showed extensive communication

with monocytes and DC, emphasizing their central role in orchestrating the immune response to retinal injury (Figure 10). These interactions imply that microglia may recruit and activate other immune cells in the early stages of retinal inflammation.

Tap1, transporter associated with antigen processing 1, plays a crucial role in the antigen presentation process by transporting peptides into the endoplasmic reticulum for loading onto MHC class I molecule^[47]. In DCs, the expression and localization of *Tap1* are significantly influenced by the maturation state of the cells^[48-49]. During DC maturation, *Tap1* relocates from early endosomes in monocytes to the ER and lysosomes in immature and mature DCs, enhancing their ability to cross-present antigens to cytotoxic T lymphocytes^[50]. This upregulation and relocalization of *Tap1* are essential for the effectiveness of DC in initiating immune responses^[47,51]. Consistently, our findings revealed that *Tap1* expression in DC was upregulated in the IR group, supporting its role in DC-mediated immune responses during RIRI (Figures 4E, 6D, 9D).

This study brings several novel insights into the understanding of RIRI. We are the first to demonstrate the critical roles of *Irf7* and *Tap1* in RIRI at both the transcriptomic and single-cell levels. Specifically, *Irf7* plays a pivotal role in the activation and polarization of microglia towards the pro-inflammatory (M1) state during the acute phase of RIRI, while *Tap1* is essential for DC maturation and antigen presentation. These findings highlight the potential of targeting *Irf7* and *Tap1* to modulate immune responses, opening new avenues for microglia-based and DC-based immunotherapies in RIRI.

Although we tried our best efforts to enhance the reliability of the findings by utilizing multiple analysis methods and validation *in vivo*, this study still has some limitations. First of all, due to the limited availability of RIRI transcriptomic datasets in public databases, our sample size is far from enough. Second, although the data sets used in this study were collected from the acute phase of RIRI, the inconsistent time points and the possible batch effect may have affected the accuracy of our results. Finally, it remains unclear how the inflammation and immune microenvironment change at different stages of RIRI (acute, subacute, and chronic phases), and how key immune regulators function throughout the process. Therefore, Future studies should focus on investigating the dynamic changes in the immune microenvironment over time and on expanding the sample size. Clinical evaluations involving both patients and healthy controls are also necessary to confirm the relationships between key immune regulators, immune infiltration, and clinical characteristics.

In conclusion, in this study we provide new insights into the molecular mechanisms of RIRI by identifying key immune-related hub genes, particularly *Irf7* and *Tap1*, which play

crucial roles in microglial activation and DC maturation. Targeting these genes may offer novel therapeutic strategies for modulating immune responses and improving clinical outcomes in the acute phase of RIRI.

ACKNOWLEDGEMENTS

Authors' Contributions: Conceptualization, Zhao H and Zhang XX; methodology, He S; software, He S; validation, He S; formal analysis, Meng TT; writing—original draft preparation, He S; writing—review and editing, Liu CY and Ren CH; funding acquisition, Zhang XX. All authors have read and agreed to the published version of the manuscript.

Data Availability: The bulk RNA-seq and scRNA-seq datasets used in this study were obtained from the BioProject database (<https://ngdc.cnbc.ac.cn/bioproject/>, the Project Accession number PRJNA859197 and PRJCA008174).

Foundation: Supported by the National Natural Science Foundation of China (No.82071312).

Conflicts of Interest: He S, None; Liu CY, None; Ren CH, None; Meng TT, None; Zhao H, None; Zhang XX, None.

REFERENCES

- 1 He S, Liu CY, Ren CH, *et al.* Immunological landscape of retinal ischemia-reperfusion injury: insights into resident and peripheral immune cell responses. *Aging Dis* 2024;16(1):115-136.
- 2 Gao Y, Wu D, Liu DC, *et al.* Novel acute retinal artery ischemia and reperfusion model in nonhuman Primates. *Stroke* 2020;51(8):2568-2572.
- 3 Tang YZ, Xiao ZB, Pan L, *et al.* Therapeutic targeting of retinal immune microenvironment with CSF-1 receptor antibody promotes visual function recovery after ischemic optic neuropathy. *Front Immunol* 2020;11:585918.
- 4 Shi HS, Ebrahim AS, Berger EA. A contrast in pathogenic responses between C57BL/6J and BALB/cJ mice using a model of retinal injury. *Am J Pathol* 2018;188(12):2717-2728.
- 5 Calugaru D. Etiology, pathogenesis, and diagnosis of neovascular glaucoma. *Int J Ophthalmol* 2022;15(6):1005-1010.
- 6 Goit RK, Taylor AW, Lo ACY. Anti-inflammatory α -melanocyte-stimulating hormone protects retina after ischemia/reperfusion injury in type I diabetes. *Front Neurosci* 2022;16:799739.
- 7 Peng YJ, Tao YC, Liu LX, *et al.* Crosstalk among reactive oxygen species, autophagy and metabolism in myocardial ischemia and reperfusion stages. *Aging Dis* 2024;15(3):1075-1107.
- 8 Chen H, Deng Y, Gan XL, *et al.* NLRP12 collaborates with NLRP3 and NLRC4 to promote pyroptosis inducing ganglion cell death of acute glaucoma. *Mol Neurodegener* 2020;15(1):26.
- 9 Yan Y, Wang ZH, Liu X, *et al.* Identification of brain endothelial cell-specific genes and pathways in ischemic stroke by integrated bioinformatical analysis. *Brain Circ* 2023;9(4):228-239.
- 10 Dou YN, Fei XW, He X, *et al.* Homer1a reduces inflammatory response after retinal ischemia/reperfusion injury. *Neural Regen Res* 2024;19(7):1608-1617.

- 11 Stark R, Grzelak M, Hadfield J. RNA sequencing: the teenage years. *Nat Rev Genet* 2019;20(11):631-656.
- 12 Hedlund E, Deng QL. Single-cell RNA sequencing: technical advancements and biological applications. *Mol Aspects Med* 2018;59:36-46.
- 13 van de Sande B, Lee JS, Mutasa-Gottgens E, *et al.* Applications of single-cell RNA sequencing in drug discovery and development. *Nat Rev Drug Discov* 2023;22(6):496-520.
- 14 Li YY, Wen YW, Liu XX, *et al.* Single-cell RNA sequencing reveals a landscape and targeted treatment of ferroptosis in retinal ischemia/reperfusion injury. *J Neuroinflammation* 2022;19(1):261.
- 15 Wingett SW, Andrews S. FastQ Screen: a tool for multi-genome mapping and quality control. *FI000Res* 2018;7:1338.
- 16 Ewels P, Magnusson M, Lundin S, *et al.* MultiQC: summarize analysis results for multiple tools and samples in a single report. *Bioinformatics* 2016;32(19):3047-3048.
- 17 Chen SF, Zhou YQ, Chen YR, *et al.* Fastp: an ultra-fast all-in-one FASTQ preprocessor. *Bioinformatics* 2018;34(17):i884-i890.
- 18 Kim D, Paggi JM, Park C, *et al.* Graph-based genome alignment and genotyping with HISAT2 and HISAT-genotype. *Nat Biotechnol* 2019;37(8):907-915.
- 19 Danecek P, Bonfield JK, Liddle J, *et al.* Twelve years of SAMtools and BCFtools. *Gigascience* 2021;10(2):giab008.
- 20 Liao Y, Smyth GK, Shi W. featureCounts: an efficient general purpose program for assigning sequence reads to genomic features. *Bioinformatics* 2014;30(7):923-930.
- 21 Love MI, Huber W, Anders S. Moderated estimation of fold change and dispersion for RNA-seq data with DESeq2. *Genome Biol* 2014;15(12):550.
- 22 Yu GC, Wang LG, Han YY, *et al.* clusterProfiler: an R package for comparing biological themes among gene clusters. *OMICS* 2012;16(5):284-287.
- 23 Gu ZG, Hübschmann D. simplifyEnrichment: a bioconductor package for clustering and visualizing functional enrichment results. *Genomics Proteomics Bioinformatics* 2023;21(1):190-202.
- 24 Sayols S. Rvgo: a Bioconductor package for interpreting lists of Gene Ontology terms. *MicroPubl Biol* 2023;2023.
- 25 Langfelder P, Horvath S. WGCNA: an R package for weighted correlation network analysis. *BMC Bioinformatics* 2008;9:559.
- 26 Finotello F, Mayer C, Plattner C, *et al.* Molecular and pharmacological modulators of the tumor immune contexture revealed by deconvolution of RNA-seq data. *Genome Med* 2019;11(1):34.
- 27 Zeng DQ, Ye ZL, Shen RF, *et al.* IOBR: multi-omics immunology biological research to decode tumor microenvironment and signatures. *Front Immunol* 2021;12:687975.
- 28 Korsunsky I, Millard N, Fan J, *et al.* Fast, sensitive and accurate integration of single-cell data with Harmony. *Nat Methods* 2019;16(12):1289-1296.
- 29 Jin SQ, Guerrero-Juarez CF, Zhang LH, *et al.* Inference and analysis of cell-cell communication using CellChat. *Nat Commun* 2021;12(1):1088.
- 30 Xu XH, Xu SL, Gao Y, *et al.* Remote ischemic conditioning slows blood-retinal barrier damage in type 1 diabetic rats. *Brain Res* 2025;1846:149253.
- 31 Teo ZL, Tham YC, Yu M, *et al.* Global prevalence of diabetic retinopathy and projection of burden through 2045: systematic review and meta-analysis. *Ophthalmology* 2021;128(11):1580-1591.
- 32 Jayaram H, Kolko M, Friedman DS, *et al.* Glaucoma: now and beyond. *Lancet* 2023;402(10414):1788-1801.
- 33 GBD 2019 Blindness and Vision Impairment Collaborators, Vision Loss Expert Group of the Global Burden of Disease Study. Causes of blindness and vision impairment in 2020 and trends over 30 years, and prevalence of avoidable blindness in relation to VISION 2020: the Right to Sight: an analysis for the Global Burden of Disease Study. *Lancet Glob Health* 2021;9(2):e144-e160.
- 34 Abcouwer SF, Shanmugam S, Muthusamy A, *et al.* Inflammatory resolution and vascular barrier restoration after retinal ischemia reperfusion injury. *J Neuroinflammation* 2021;18(1):186.
- 35 Shahror RA, Morris CA, Mohammed AA, *et al.* Role of myeloid cells in ischemic retinopathies: recent advances and unanswered questions. *J Neuroinflammation* 2024;21(1):65.
- 36 Chen Q, Sun LJ, Chen ZJ. Regulation and function of the cGAS-STING pathway of cytosolic DNA sensing. *Nat Immunol* 2016;17(10):1142-1149.
- 37 Cai X, Chiu YH, Chen ZJ. The cGAS-cGAMP-STING pathway of cytosolic DNA sensing and signaling. *Mol Cell* 2014;54(2):289-296.
- 38 Andreeva K, Zhang MX, Fan W, *et al.* Time-dependent gene profiling indicates the presence of different phases for ischemia/reperfusion injury in retina. *Ophthalmol Eye Dis* 2014;6:43-54.
- 39 Hagemeyer N, Prinz M. Burning down the house: IRF7 makes the difference for microglia. *EMBO J* 2014;33(24):2885-2886.
- 40 Gadagkar SG, Lalancette-Hébert M, Thammisetty SS, *et al.* CD36 neutralisation blunts TLR2-IRF7 but not IRF3 pathway in neonatal mouse brain and immature human microglia following innate immune challenge. *Sci Rep* 2023;13(1):2304.
- 41 Cohen M, Matcovitch O, David E, *et al.* Chronic exposure to TGFβ1 regulates myeloid cell inflammatory response in an IRF7-dependent manner. *EMBO J* 2014;33(24):2906-2921.
- 42 Tanaka T, Murakami K, Bando Y, *et al.* Interferon regulatory factor 7 participates in the M1-like microglial polarization switch. *Glia* 2015;63(4):595-610.
- 43 Li ZZ, Huang QM, Chen HP, *et al.* Interferon regulatory factor 7 promoted glioblastoma progression and stemness by modulating IL-6 expression in microglia. *J Cancer* 2017;8(2):207-219.
- 44 Holtman IR, Skola D, Glass CK. Transcriptional control of microglia phenotypes in health and disease. *J Clin Invest* 2017;127(9):3220-3229.
- 45 Xu SB, Mei SH, Lu JN, *et al.* Transcriptome analysis of microglia reveals that the TLR2/IRF7 signaling axis mediates neuroinflammation after subarachnoid hemorrhage. *Front Aging Neurosci* 2021;13:645649.

- 46 Salkar A, Wall RV, Basavarajappa D, *et al.* Glial cell activation and immune responses in glaucoma: a systematic review of human postmortem studies of the retina and optic nerve. *Aging Dis* 2024;15(5):2069-2083.
- 47 López-Albaitero A, Mailliard R, Hackman T, *et al.* Maturation pathways of dendritic cells determine TAP1 and TAP2 levels and cross-presenting function. *J Immunother* 2009;32(5):465-473.
- 48 Erra Diaz F, Mazzitelli I, Bleichmar L, *et al.* Concomitant inhibition of PPAR γ and mTORC1 induces the differentiation of human monocytes into highly immunogenic dendritic cells. *Cell Rep* 2023;42(3):112156.
- 49 Schinnerling K, García-González P, Aguillón JC. Gene expression profiling of human monocyte-derived dendritic cells - searching for molecular regulators of tolerogenicity. *Front Immunol* 2015;6:528.
- 50 Barends M, Koller N, Schölz C, *et al.* Dynamic interactome of the MHC I peptide loading complex in human dendritic cells. *Proc Natl Acad Sci U S A* 2023;120(25):e2219790120.
- 51 Döring M, Blees H, Koller N, *et al.* Modulation of TAP-dependent antigen compartmentalization during human monocyte-to-DC differentiation. *Blood Adv* 2019;3(6):839-850.